Resonantly excited exciton dynamics in two-dimensional $MoSe_2$ monolayers

L. Scarpelli,[1] F. Masia,[1] E. M. Alexeev,[2] F. Withers,[3] A. I. Tartakovskii,[2] K. S. Novoselov,[4] and W. Langbein[1]

[1]*School of Physics and Astronomy, Cardiff University, The Parade, Cardiff CF24 3AA, United Kingdom*

[2]*Department of Physics and Astronomy, University of Sheffield, Hounsfield Rd, Sheffield S3 7RH, United Kingdom*

[3]*College of Engineering, Mathematics and Physical Sciences, University of Exeter, North Park Rd, Exeter EX4 4QF United Kingdom*

[4]*School of Physics and Astronomy, University of Manchester, Oxford Rd, Manchester M13 9PL, United Kingdom*

(Received 11 April 2017; revised manuscript received 5 June 2017; published 7 July 2017)

We report on the exciton and trion density dynamics in a single layer of $MoSe_2$, resonantly excited and probed using three-pulse four-wave mixing (FWM), at temperatures from 300 K to 77 K. A multiexponential third-order response function for amplitude and phase of the heterodyne-detected FWM signal including four decay processes is used to model the data. We provide a consistent interpretation within the intrinsic band structure, not requiring the inclusion of extrinsic effects. We find an exciton radiative lifetime in the subpicosecond range consistent to what has been recently reported by Jakubczyk *et al.* [Nano Lett. **16**, 5333 (2016)]. After the dominating radiative decay, the remaining exciton density, which has been scattered from the initially excited direct spin-allowed radiative state into dark states of different nature by exciton-phonon scattering or disorder scattering, shows a slower dynamics, covering 10-ps to 10-ns time scales. This includes direct spin-allowed transitions with larger in-plane momentum, as well as indirect and spin-forbidden exciton states. We find that exciton-exciton annihilation is not relevant in the observed dynamics, in variance from previous finding under nonresonant excitation. The trion density at 77 K reveals a decay of the order of 1 ps, similar to what is observed for the exciton. After few tens of picoseconds, the trion dynamics resembles the one of the exciton, indicating that trion ionization occurs on this time scale.

DOI: 10.1103/PhysRevB.96.045407

I. INTRODUCTION

Single layers (SL) of transition metal dichalcogenides (TMD) can be direct band-gap semiconductors, with the band gap at the valleys located in the corners K of the hexagonal Brillouin zone [1,2]. The spin-orbit interaction and lacking inversion symmetry result in a spin splitting of the electron and hole bands at the two nonequivalent valleys $\pm$K, linking the circular polarization of the transition to the valley index $\pm$ [3,4]. Therefore, excitons are generated in the +K (−K) valley by absorption of right (left)-handed light, respectively. Due to the reduced screening of the Coulomb interaction and the two-dimensional (2D) confinement, excitons in SL-TMD have a large binding energy of a few hundred meV [5]. For the same reason, exciton-exciton interaction is expected to be enhanced, and the effect of exciton-exciton annihilation (EEA) has been reported [6–8]. The spin-orbit interaction splits the spin states at the valleys by a few hundred meV [9] in the valence band (VB), and by a few tens of meV [10] in the conduction band (CB). The exciton transition between the lower CB and higher VB valley is called A exciton (X_A) while the transition between the higher CB and lower VB is called B exciton (X_B) and has the opposite circular polarization. Mixed transitions are spin forbidden, and transitions between different valleys are momentum forbidden and thus called "dark". The exciton dynamics therefore depends strongly on the distribution and the scattering between the different dark and bright states and their dispersion [11]. The energy of such dark states depends on the TMD under consideration. In WX_2, where X = S,Se, optically dark states appear to have a lower energy than bright states, while the opposite is suggested by experiments on MoX_2 [10,12]. Dark states are thought to be responsible [13] for the anomalous polarization response observed in SL-$MoSe_2$ [14,15]. The role of dark states in the exciton dynamics is an important open issue in the understanding of the carrier dynamics. Indeed, recent experiments on both $MoSe_2$ and WSe_2 have considered intrinsic dark states to describe the exciton dynamics [16,17]. Population of dark states can occur by exciton-phonon as well as exciton-exciton scattering through many different mechanisms [18]. Electron-hole exchange interaction further affects the dynamics by introducing additional energy differences between spin 1 (spin forbidden) and spin 0 (spin-allowed) exciton states [19]. In the present work, we report on resonantly excited exciton and trion density dynamics in a single layer of $MoSe_2$. Importantly, resonant excitation suppresses the influence of free carriers, which complicates the dynamics in nonresonantly excited photoluminescence or pump-probe studies. Furthermore, in these studies, the influence of excitons distributed over and relaxing across the large variety of dark states onto the bright states is measured. Heterodyne detected four-wave mixing (FWM) instead can distinguish pump and probe also for degenerate resonant excitation, allowing us to probe the initial dynamics of the optically coupled states, including their dephasing, and provides a well-defined initial exciton distribution for the subsequent density dynamics. The paper is organized as follows: In Sec. II details on the experimental technique and on the investigated sample are given. In Sec. III measurements of dephasing time of X_A and the related trion transition are shown for different temperatures. In Sec. IV density dynamics probed at the X_A transition as function of density (Sec. IV A) and temperature (Sec. IV B) are shown and analyzed, and in Sec. IV C an interpretation of the observed dynamics in terms of the intrinsic band structure is put forward. In Sec. IV D the density-dependent dynamics is analyzed for exciton Auger recombination, and no evidence for EEA is found. Finally, in Sec. V, we discuss experiments resonant to the trion and in Sec. VI we summarize our results.

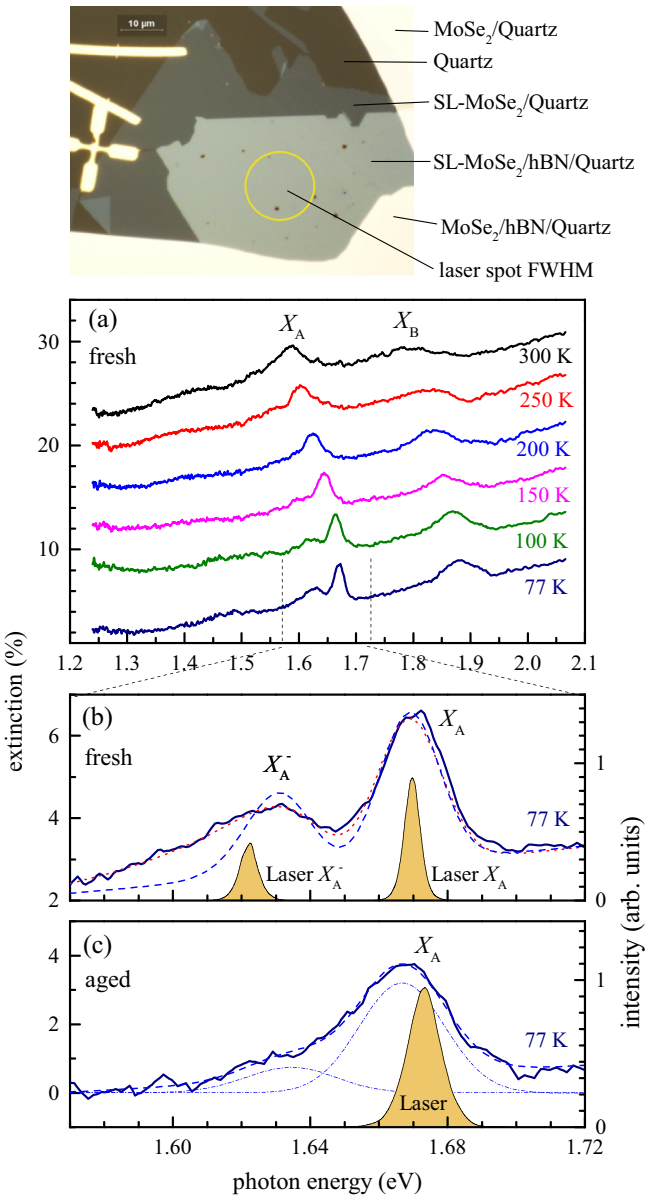

FIG. 1. Sample characterization and excitation laser spectra. (Top) Reflection image of the investigated sample, taken with a 0.8 numerical aperture. The different regions are labeled. (a) Extinction of the fresh sample as function of temperature, vertically offset for clarity. (b) Zoom of extinction at $T = 77$ K, together with the excitation laser spectrum. Panel (c) as panel (b) but for the aged sample. Dashed lines are fits of the data (see text).

II. SAMPLE AND EXPERIMENTAL SETUP

The sample analyzed in this work is a SL-$MoSe_2$ transferred onto a hexagonal boron nitride (hBN) layer on a 1-mm-thick c-cut quartz substrate. A reflection image is given in the top of Fig. 1. The investigated SL has a size of about $50 \times 70\ \mu m^2$. The sample is covered by a second 1-mm-thick c-cut quartz substrate to provide thermal radiation screening and mechanical protection, and mounted in a flow cryostat, onto the cold finger in vacuum.

The extinction of the sample was measured using white-light transmission, referenced to the quartz region adjacent to the investigated flake. The sample was stored in vacuum and measured 6 months after preparation ("fresh") and 3 months afterwards, after a few thermal cycles ("aged"). The extinction of the fresh sample as function of temperature during the first cooldown is given in Fig. 1(a). The spectra show the X_A and X_B absorption peaks, which are shifting to higher energies with decreasing temperature, as expected. At $T = 77$ K, a peak below the X_A is observed which is attributed to the X_A trion absorption. We call the trion here X_A^-, assuming a negative charge. Negatively and positively charged trions have very similar binding energies [20]. The trion absorption forms due to the presence of electrons at the edge of the conduction band. The trion absorption observed here shows a low energy tail [see also Fig. 1(b)]. In principle, a low-energy tail is expected for the transition from the thermalized free carrier distribution [20,21]. The trion lineshape in absorption has recently been studied [22] in a charge-tunable structure at a temperature of $T = 4$ K, at which the thermal energy of $k_B T \approx 0.34$ meV is much smaller than the line broadening and such a tail is not observed as expected. At the higher temperature of $T = 77$ K used here, $k_B T \approx 6.6$ meV and thus could be relevant. We have fitted the absorption lineshape $A(\hbar\omega)$ using the function

$$A(x) = C_0 + C_1 x + A_X \exp\left[-\left(\frac{x - E_X}{\sqrt{2}\sigma}\right)^2\right] + \frac{A_T}{2}\left[1 - \mathrm{erf}\left(\frac{x - E_T}{\sqrt{2}\sigma} + \frac{C\sigma}{\sqrt{2}k_B T}\right)\right] \times \exp\left[C\frac{x - E_T}{k_B T} + \left(\frac{C\sigma}{\sqrt{2}k_B T}\right)^2\right]. \quad (1)$$

C_0 and C_1 provide a baseline, A_X is the amplitude of the Gaussian exciton peak of position E_X, A_T is the amplitude of the trion lineshape of position E_T, and $C = M_T^*/M^*$ is the ratio between the trion effective mass $M_T^* = 2m_e^* + m_h^*$ and the exciton effective mass $M^* = m_e^* + m_h^*$. Using the electron effective mass [23] $m_e^* = 0.53\, m_0$ and the hole effective mass $m_h^* = 0.65\, m_0$, we find $C \approx 1.45$. The width σ is the inhomogeneous broadening of exciton and trion, and the trion lineshape is convoluted with an exponential decay due to the thermal electron energy distribution and momentum conservation during absorption [20,21]. For simplicity we have neglected the electron-energy dependence of the matrix element [20]. Using a Gaussian assumes that the absorption lineshape is dominated by the inhomogeneous broadening, which is confirmed by the measured homogeneous broadening (see Sec. III). Using the same inhomogeneous broadening σ for exciton and trion is reasonable, since the influence of the electron on the exciton wave function is small, as shown by the electron binding energy in the trion being an order of magnitude below the exciton binding energy. A fit to the extinction of the fresh sample [see blue dashed line Fig. 1(b)] shows that the resulting low-energy tail of the trion is less extended than observed. We find a trion binding energy of $E_X - E_T \approx 34$ meV and a full width at half maximum (FWHM) of the exciton peak of $2.355\sigma \approx 20$ meV. Leaving C as free parameter (see red dotted curve), a good fit is obtained, yielding

$C = 0.18$, a trion binding energy of 27 meV and a FWHM of 22 meV.

A fit to the extinction of the aged sample [see the blue dashed line in Fig. 1(c)] with $C = 1.45$ shows good agreement with the data, providing a trion binding energy of 28 meV and a FWHM of 29 meV. The retrieved trion binding energies are consistent with previous reports [20,24–27]. The aged sample shows a larger linewidth and a smaller trion contribution. This is about 25% of the exciton peak area, against 63% for the fresh sample using the fit with $C = 1.45$. The microscopic origin of the change is unknown—one could speculate that it is due to a wrinkling of the sample after thermal cycling, which creates a larger strain inhomogeneity and different dielectric environments. An inhomogeneous distribution of strain and trion concentration was recently shown on SL-$MoSe_2$ on Si/SiO_2 substrates [26]. We will report measurements on both samples in this paper.

In order to measure the exciton density and dephasing dynamics, we perform three-pulse FWM spectroscopy. The excitation pulses are derived from a femtosecond Ti:sapphire laser (Coherent Mira 900) with 76-MHz repetition rate. The pulse spectra used are given in Fig. 1(b) and Fig. 1(c) and show a FWHM of 5.5 meV and 11 meV, corresponding to pulse durations of 240 fs and 120 fs, respectively. The pulses are focused onto the sample to a spot of about 16-μm intensity FWHM. The first pulse (P_1) induces a coherent polarization in the sample, which after a delay τ_{12} is converted into a density grating by the second pulse (P_2). The third pulse (P_3), delayed by τ_{23} from P_2, is diffracted by this density grating, yielding the FWM signal. In the employed heterodyne technique [28], the pulse trains are radio-frequency shifted resulting in a frequency-shifted FWM field which is detected by its interference with a reference pulse. In the investigated inhomogeneously broadened ensemble, the FWM signal is a photon echo emitted at a time τ_{12} after P_3, and the microscopic dephasing is inferred from the decay of the photon echo amplitude versus τ_{12}. Conversely, the decay of the photon-echo amplitude versus τ_{23} probes the exciton density dynamics [29]. This setup was used in previous works [30–32], and more details can be found in the supplement of Ref. [32]. For all the data shown in this work, each beam had equal power P. The polarization of the beams was controlled by waveplates. The polarization configuration of P_1, P_2, P_3 and detection will be abbreviated by four symbols in this order, e.g., $(\rightarrow,\rightarrow,\uparrow,\uparrow)$ for cross-linear polarization of $P_{1,2}$ to P_3 and detection. The repetition rate of the excitation corresponds to a period T_r of about 13 ns, which limits the maximum relaxation time which can be extracted from the delay time dependence. Furthermore, the density modulation frequency of $(\Omega_1 - \Omega_2)/(2\pi) = 1$ MHz provides a single pole high-pass filter for the response, with a cutoff at lifetimes of $1/(\Omega_1 - \Omega_2) \sim 160$ ns.

III. EXCITON AND TRION DEPHASING

The dephasing of X_A and X_A^- was measured by FWM using $(\rightarrow,\rightarrow,\uparrow,\uparrow)$ polarization on the fresh sample. The measured photon echo amplitude versus τ_{12} is shown in Fig. 2. We can see a rapid decay of the echo amplitude

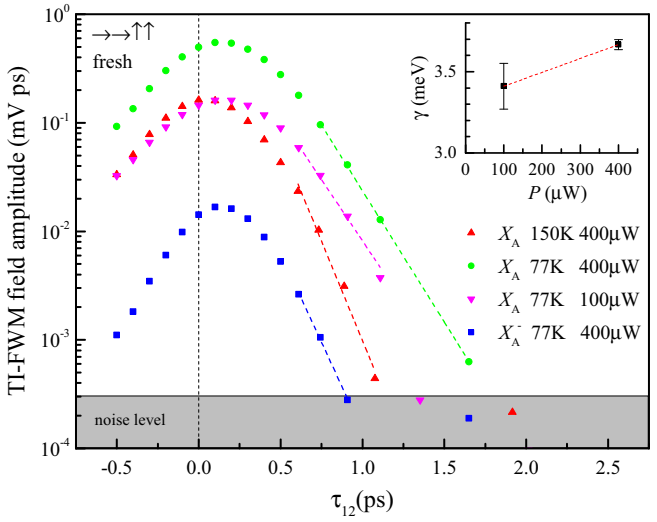

FIG. 2. X_A and X_A^- time-integrated four-wave mixing (TI-FWM) field amplitude as a function of τ_{12} for different temperatures and excitation powers and τ_{23} of 1 ps and 1.2 ps, respectively, measured for the fresh sample. The dashed lines are exponential fits to the data. The inset shows the extracted power dependence of the X_A homogeneous linewidth γ at $T = 77$ K.

with τ_{12}. Since the laser pulse spectrum is narrower than the broadening of the transitions [see Fig. 1(b)], the photon echo duration is given by the laser pulse width. To extract the dephasing time T_2, we fit the data beyond pulse overlap $\tau_{12} > 0.5$ ps with an exponential decay $\propto \exp(-2\tau_{12}/T_2)$. From the fits, shown as dashed lines in Fig. 2, we obtain for X_A at $T = 77$ K a dephasing time T_2 of (386 ± 16)fs for $P = 100$ μW and of (359 ± 3)fs for $P = 400$ μW. At 150 K and for $P = 400$ μW we obtain a T_2 of (237 ± 18) fs. The data for 150 K is close to the limit of the time resolution of the experiment. The extracted exciton homogeneous linewidth $\gamma = 2\hbar/T_2$ shows a weak power dependence (see inset of Fig. 2), which we fitted using $\gamma = \gamma_0 + \gamma_P P$. We find a zero-density homogeneous linewidth γ_0 of 3.3 meV and $\gamma_P \approx 1$ meV/mW.

The exciton dephasing in SL-$MoSe_2$ is affected by radiative decay and scattering by phonons and charge carriers. The trion absorption found in Sec. II shows the presence of charge carriers, which creates an additional dephasing and relaxation channel for excitons. In Ref. [33], the temperature dependent linewidth (FWHM) of the X_A resonance in reflection was fitted with

$$\gamma(T) = \gamma_0 + \frac{A}{e^{E_A/k_B T} - 1} \tag{2}$$

using $A = 72$ meV and $E_A = 30$ meV. This width includes homogeneous and inhomogeneous broadening. The phonon activated term, representing a homogeneous broadening, amounts to 33 meV at $T = 300$ K, 7.8 meV at $T = 150$ K, and 0.79 meV at $T = 77$ K. In Ref. [26], an additional linear term of 0.03 meV/K was found, and a homogeneous broadening of about 3.5 meV at 77 K, which is consistent with our finding.

The trion X_A^- shows a faster dephasing than X_A, with $T_2 = (266 \pm 13)$ fs at $T = 77$ K, corresponding to a homogeneous broadening of (5.0 ± 0.3) meV. This is attributed to

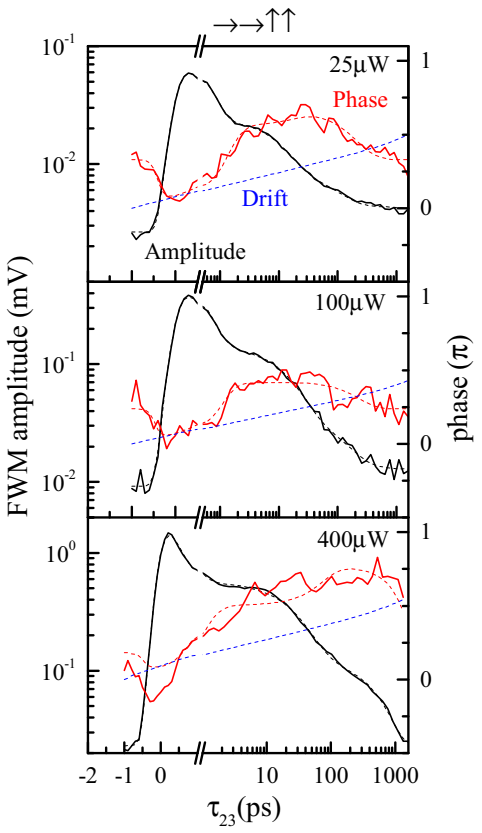

FIG. 3. Density dynamics of the fresh sample. FWM field amplitude (black solid line) and phase (red solid line) as function of the delay τ_{23} for different excitation powers P as given and cross-linear polarization configuration $(\rightarrow,\rightarrow,\uparrow,\uparrow)$. The dashed lines are fits to the data. The fitted phase drift (blue dashed line) has been subtracted from the data. Excitation resonant to X_A at $T = 77$ K.

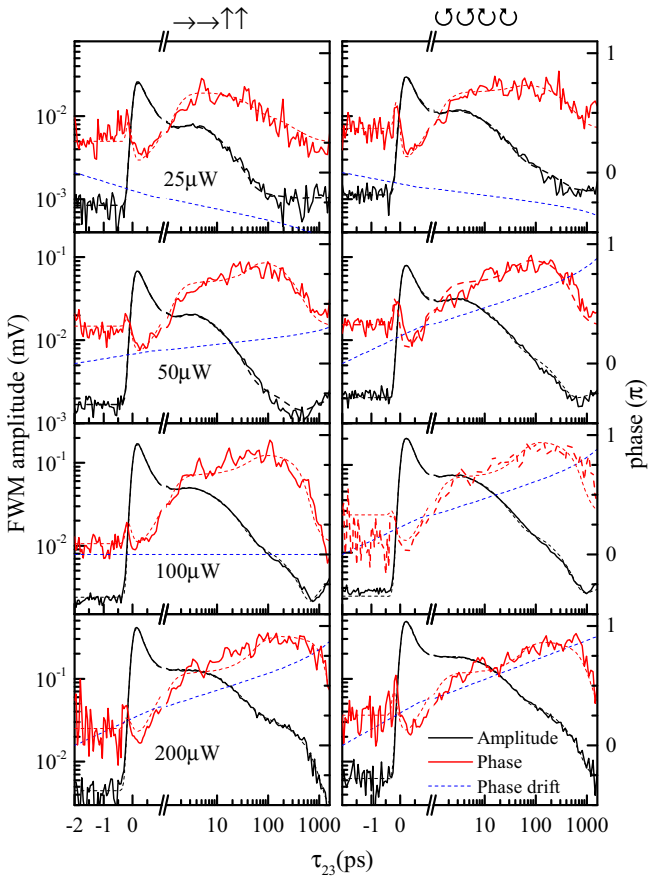

FIG. 4. As Fig. 3, but for the aged sample and two polarization configurations, cross-linear $(\rightarrow,\rightarrow,\uparrow,\uparrow)$ and cross-circular (↺ ↺↻↻).

the additional carrier, the charged character, and the lower binding energy, increasing the scattering rate.

IV. EXCITON POPULATION DYNAMICS

In this section, we discuss the measured FWM density dynamics as a function of τ_{23} for $\tau_{12} = 0$ ps after resonantly exciting A-excitons X_A.

A. Density dependence

The measured FWM field amplitude and phase for different excitation power P are shown in Fig. 3 for the fresh sample and in Fig. 4 for the aged sample for linear and circular polarization configurations over four orders of magnitude in delay τ_{23}. We find processes with time scales from the picosecond to the nanosecond range. To quantitatively analyze the data, we use a fit with the complex multiexponential response function

$$R(\tau) \propto A_{\rm nr} e^{i\varphi_{\rm nr}} \delta(\tau) + \sum_n A_n \theta(\tau) \exp\left(i\varphi_n - \frac{\tau}{\tau_n}\right), \quad (3)$$

where A_n, φ_n, and τ_n are amplitude, phase, and decay time of the nth decay process and $A_{\rm nr}$ is a nonresonant instantaneous component such as Kerr effect or two-photon absorption. Equation (3) describes the FWM complex field as a coherent superposition of exponential decay components created by the pump. Using a complex fit takes into account the different phases of the components, given by the relative effect on absorption and refractive index. The measurements, see, for example, $P = 100$ μW in Fig. 4, show a characteristic change of the phase versus time—the phase at negative delays is similar to the phase of the resonantly generated signal after pulse overlap, at $\tau_{23} > 100$ fs. This component decays in the first picoseconds after which a phase change of about $\pi/2$ is observed together with a slower dynamics. After around 20 ps a second, a somewhat smaller phase shift is seen, and, later, around 1 ns, the phase starts to shift back to its initial value. The measured phase contains a slow drift, which is caused by temperature drift of the setup, changing the relative phase of reference and probe pulses over the time t of the measurement of a few minutes. This phase drift has been included in the fitting procedure in a prefactor $\exp[i(\varphi_0 + \varphi_0' t)]$ using a linear time dependence. In the fit, four components $n = 1..4$ are used. We fix the phase of the fastest component to $\varphi_1 = 0$ so the phases of the other components represent the relative phases to the first component. The response is convoluted with a periodic Gaussian to reflect the excitation pulses of FWHM $2\sqrt{\ln 2}\tau_0$ in amplitude, and repetition period T_r, yielding

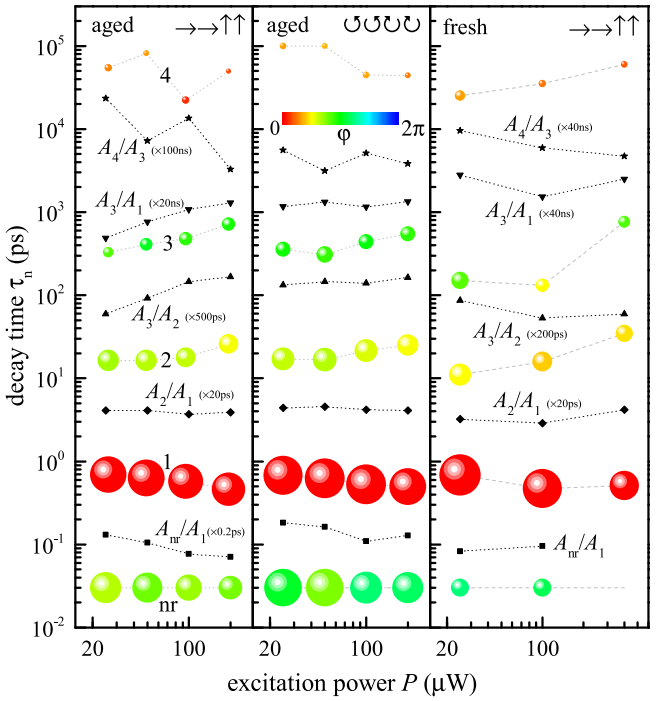

FIG. 5. Results of the fit of Eq. (4) to the data shown in Fig. 3 and Fig. 4. The amplitudes A_n normalized to the third-order scaling $P^{3/2}$ with the excitation power are given by the volume of the symbol (diameter proportional to $A_n^{1/3}P^{-1/2}$ and for absolute scaling $A_1 = 40\ \mu$V at $P = 25\ \mu$W for the aged $(\rightarrow,\rightarrow,\uparrow,\uparrow)$ sample and 108 μV for the fresh sample). The phases φ_n are given by the symbol color according to the color map. A_{nr} is shown at a decay time of 30 fs. Selected amplitude ratios, scaled as labeled, are given as symbols. Dotted lines are guides for the eye.

the fit function

$$F(t,\tau) = \exp[i(\varphi_0 + \varphi_0' t)]\Bigg(A_{nr}\exp\left(i\varphi_{nr} - \frac{\tau^2}{\tau_0^2}\right) + \sum_n A_n\left\{\frac{1}{e^{\frac{T_r}{\tau_n}} - 1} + \frac{1}{2}\left[1 + \mathrm{erf}\left(\frac{\tau}{\tau_0} - \frac{\tau_0}{2\tau_n}\right)\right]\right\} \times \exp\left(i\varphi_n + \frac{\tau_0^2}{4\tau_n^2} - \frac{\tau}{\tau_n}\right)\Bigg), \quad (4)$$

which includes the pile-up of signal due to the finite T_r. The resulting fits are given in Fig. 3 for the fresh and Fig. 4 for the aged sample. In the figure, we show for clarity the phase corrected for the phase drift, and the phase drift separately.

The decay times τ_n, amplitudes A_n, and phases φ_n resulting from the fit to the complex data are shown in Fig. 5. The amplitudes are shown normalized to the scaling $P^{3/2}$ expected for a $\chi^{(3)}$ process. The fastest component with $\tau_1 \sim 0.6$ ps represents the dominating amplitude A_1, about 5 times larger $(A_1/A_2 \sim 5)$ than the second component with $\tau_2 \sim 20$ ps and a phase of $\varphi_2 \sim \pi/2$. The next component with $\tau_3 \sim 400$ ps has an amplitude A_3 which is again about 4 times lower than A_2, $(A_2/A_3 \sim 4)$, and a phase of $\varphi_3 \sim \pi$, i.e., it is out of phase to the first component. The fourth component with $\tau_4 \sim 20..100$ ns has an amplitude which is about 10 times lower than A_3, $(A_3/A_4 \sim 10)$. It is longer than T_r and is

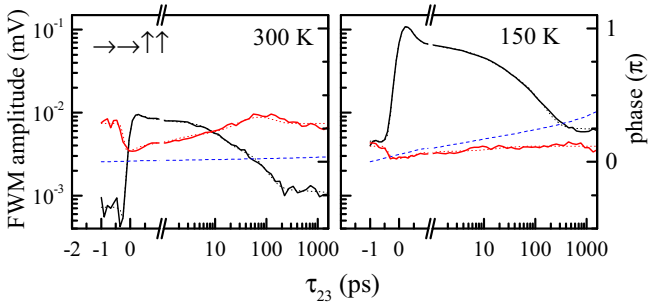

FIG. 6. Density dynamics of the fresh sample for different temperatures as indicated. FWM field amplitude and phase as function of the delay τ_{23} for $P = 100\ \mu$W, cross-linear $(\rightarrow\rightarrow\uparrow\uparrow)$ polarization configuration, and excitation resonant to X_A.

responsible for the signal at negative delay due to a pile-up of previous repetitions. It has a phase $\varphi_4 \sim 0..\pi/4$, i.e., similar to the initial component.

We observe a weak dependence of the dynamics on the excitation power. With P increasing over an order of magnitude, τ_1 is decreasing by a few 10%, and τ_2 and τ_3 are increasing by about a factor of 2. The dominant amplitude A_1 is scaling as expected for a third-order process, as seen by the near constant symbol size versus P, apart from the highest powers used. The ratio A_2/A_1 does not change with P, but the ratio A_3/A_2 is increasing by a factor of 2 for the cross-linear aged case, near constant for the cross-circular aged case, and slightly decreasing for the cross-linear fresh case. For the longest component the values of τ_4 and A_4 are partially correlated since the signal measured at negative delay is given by a combination of both, and at the maximum positive delay of 1.6 ns a part of component 3 still is remaining.

B. Temperature dependence

To investigate the influence of phonon-scattering and thermal distribution across states, we have measured the density dynamics for different temperatures. Additionally to the $T = 77$ K data shown in Fig. 3, for which the thermal energy $k_B T$ is about 6.6 meV, we have taken data for 150 K and 300 K, corresponding to $k_B T$ of 13 meV and 26 meV, respectively. A power $P = 100\ \mu$W was used, allowing for sufficient dynamic range while limiting the density-induced effects. The resulting dynamics is given in Fig. 6. The excitation pulse center wavelength was shifted to match the X_A for each temperature, compensating the temperature dependence of the band gap.

We find that with increasing temperature, the main effect is a reduction of the decay in the first picosecond, while the subsequent dynamics is changing in a more subtle way. The results of a fit of the data with the multiexponential decay model are given in Fig. 7.

We see the reduction of A_1 with increasing temperature as expected and an acceleration of the third component from $\tau_3 \sim 130$ ps at 77 K to 55 ps at 300 K.

C. Discussion

To interpret the results, we remind ourselves that the strong exciton binding energy of a few hundred meV, combined

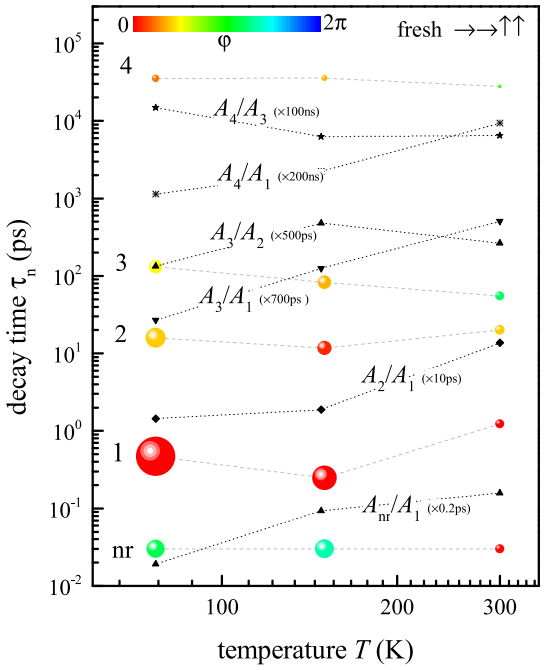

FIG. 7. As Fig. 5, but for the fresh sample only, as function of temperature for $P = 100\ \mu$W and cross-linear ($\rightarrow\rightarrow\uparrow\uparrow$) polarization configuration.

with resonant excitation of the lowest exciton X_A, leads to a dominating role of excitons in the carrier dynamics. Free electron-hole pairs are expected to play a minor role, even at room temperature. Furthermore, for the same reason, the lower spin-split valence band, with a splitting energy of about 200 meV, involved in X_B, is also expected to be not relevant. In the presence of extrinsic carriers, due to defects or doping, the resulting electron or hole density leads to the formation of trion states. These will be considered later.

The remaining intrinsic states expected to be relevant to the exciton dynamics are sketched in Fig. 8. First, the excitons have an in-plane dispersion [see Fig. 8(a)] given by their center-of-mass (COM) mass M^*, the sum of electron and hole effective masses, and $M^* \sim m_0$ [23]. We note here that the prediction [19] of a Dirac-cone type exciton dispersion in the light cone is disputed [34,35]. Neglecting in-plane disorder, the exciton states are eigenstates of the in-plane wave vector $\mathbf{K}_{||}$. They couple to external propagating light only if they are "slow", having a $\mathbf{K}_{||}$ within the light cone, i.e., $|\mathbf{K}_{||}| < K_0 = n\omega/c$, where n is the refractive index of the surrounding medium, as is well established for quantum well excitons [36,37]. We will use here $n = 1.5$ from the quartz substrate and superstrate. A similar value is obtained considering instead SL-$MoSe_2$ sandwiched between hBN with $n \sim 2$ and vacuum. Excitons having a $\mathbf{K}_{||}$ outside the light cone, which we call "fast" here, couple to evanescent fields which results in a polariton energy shift [34] of similar magnitude as the radiative linewidth inside the light cone, as shown in the right side of the sketch. The polariton interaction creates exciton eigenstates which are linearly polarized along or orthogonal to $\mathbf{K}_{||}$, called longitudinal (L) and transversal (T) exciton-polaritons. The exciton radiative lifetime within the radiative cone τ_r scales with the square of the exciton oscillator strength and is about

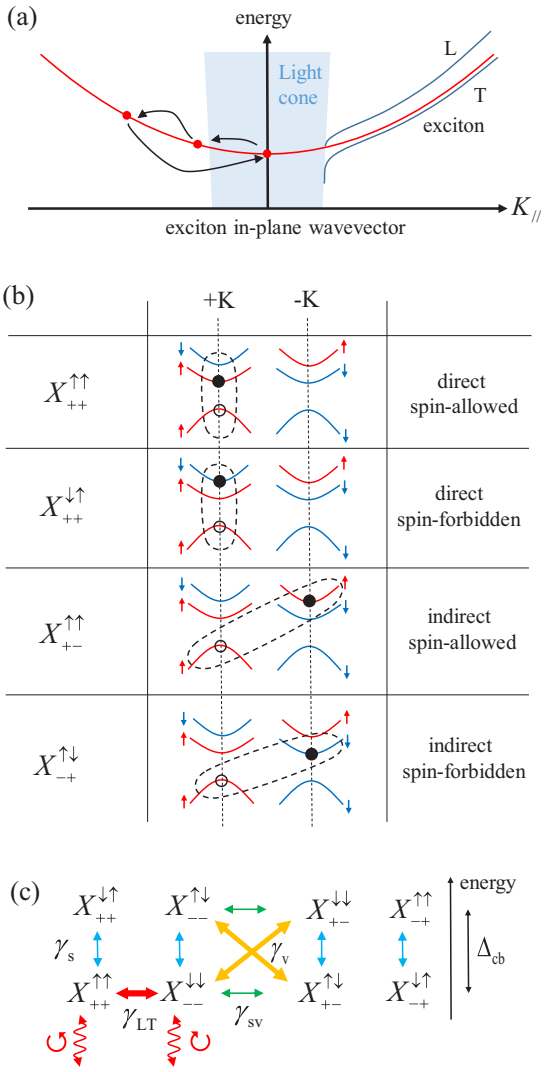

FIG. 8. (a) Sketch of the exciton center-of-mass dispersion, and phonon-assisted scattering between inside and outside the light cone; (b) possible electron-hole combinations in the single-particle electronic band structure forming the exciton. An occupied (unoccupied) electron state is represented by full (empty) black circle, with a red/blue vertical arrow indicating the corresponding electron spin. The nomenclature and properties of each exciton state is given. The lower energy valence band with opposite spin is not shown due to its large energy splitting of about 200 meV. Each state shown has degenerate partner with inverted indices, e.g., $X^{\uparrow\uparrow}_{++}$ and $X^{\downarrow\downarrow}_{--}$; (c) sketch of the scattering rates between the exciton states, as explained in text. Δ_{cb} is the energy splitting between CB and VB. Wavy red lines indicate radiative recombination with emission of circularly polarized light.

10 ps in the classical 2D system—GaAs quantum wells [37]. The large exciton binding energy in SL-$MoSe_2$ leads to a faster lifetime in the sub-picosecond regime [16,26,35,38]. This situation is similar to the fast radiative lifetimes in the 1 ps range observed in two-dimensional CdSe platelets [32], which have an exciton binding energy of 100–300 meV. In the presence of in-plane disorder, the eigenstates have a finite width in $\mathbf{K}_{||}$, yielding longer minimum radiative lifetimes, as

only part of the localized exciton wave function is within the radiative cone [39]. Scattering between slow and fast excitons can occur by interaction with phonons, excitons, and charge carriers. Assuming thermal equilibrium within the exciton dispersion, one can define [35,37] an effective radiative decay time of

$$\tau(T) = \frac{3k_B T}{4E_0}\tau_r, \quad \text{with } E_0 = \frac{\hbar^2 K_0^2}{2M^*} \tag{5}$$

with the exciton kinetic energy at the edge of the light cone $E_0 = 4.5\ \mu$eV. Note that in this expression the polariton shift and local disorder effects are neglected, which should be a reasonable approximation for $k_B T$ much larger than the relevant energy scales of a few meV. This expression yields the values $\tau(77\ K) \approx 1100\ \tau_r \approx 440$ ps, $\tau(150\ K) \approx 2150\ \tau_r \approx 860$ ps, and $\tau(300\ K) \approx 4310\ \tau_r \approx 1.7$ ns, using [38] $\tau_r = 0.4$ ps. The assumed thermalization in this model requires that the scattering is much faster than τ_r, which is not the case at $T = 77$ K for which we measure a dephasing time of about 0.36 ps (see Sec. III). We therefore expect at this temperature a two component decay, first the fast radiative decay of the initially excited slow excitons, and later a decay of the fast excitons, via scattering to the slow excitons and subsequent radiative emission. The resulting decay rate is lower than predicted in the thermalized case due to the sub-thermal population of states inside the radiative cone. At room temperature instead, the phonon scattering is likely to be sufficiently fast to allow thermalization. Accounting for disorder, leading to in-plane localization, the maximum radiative rate of the exciton states decreases [39,40], allowing for better thermalization. The effect of inhomogeneous broadening on the dephasing has recently been shown [26]. This broadening will depend on the specific sample investigated, as it is related to the influence of the embedding layers.

Further to the in-plane dispersion, the exciton has different spin and valley states [3,13], as sketched in Fig. 8(b). We denote these states as $X^{s_e s_h}_{i_e i_h}$, where i_e and i_h are the valley index $+$ or $-$, and s_e and s_h are the spin $\uparrow$ or $\downarrow$, of the electronic state, of electron and hole, respectively. The optical transitions are circularly polarized according to the valley index, and conserve spin and valley index. We call an exciton state spin-allowed for $s_e = s_h$, and spin-forbidden otherwise. Furthermore, an exciton which has equal valley index $i_e = i_h$ is called direct, and indirect otherwise. The direct spin-allowed states $X^{\uparrow\uparrow}_{++}$ and $X^{\downarrow\downarrow}_{--}$ couple to external light, and thus have a radiative decay, and the polariton features discussed above. Notably, the polariton self-energy is coupling these two states to form linearly polarized superpositions L and T, with a splitting of a few meV for the fast excitons [34]. This splitting corresponds to an oscillation between $X^{\uparrow\uparrow}_{++}$ and $X^{\downarrow\downarrow}_{--}$ on the picosecond time scale, which can explain the observed fast spin relaxation [25] and is indicated by γ_{LT}. Note that the eigenstates and splitting depend on $\mathbf{K}_{||}$, so instead of a beating a fast decay can be expected. Including in-plane disorder, the LT splitting is transformed into a fine-structure splitting of the disorder-localized exciton states, providing a fast spin relaxation without dephasing [41].

The direct spin-forbidden states $X^{\downarrow\uparrow}_{++}$ and $X^{\uparrow\downarrow}_{--}$ are assumed to have higher energy due to the conduction band splitting of about [13] $\Delta_{cb} = 20$ meV. The direct spin-forbidden states $X^{\uparrow\downarrow}_{++}$ and $X^{\downarrow\uparrow}_{--}$ are not considered in this discussion due to the large valence band splitting. The electron-hole exchange interaction is expected to lead to an energy splitting of the degenerate direct spin-allowed and indirect spin-forbidden excitons but reliable measurements or calculations of this effect are not available to our knowledge.

Scattering between the different states can occur via phonon absorption or emission. The phonon band structure is given in Ref. [23]. A sketch of the different scattering rates considered is given in Fig. 8(c). One can distinguish scattering changing the valley only, denoted by γ_v; scattering changing the spin only, denoted by γ_s; and scattering changing both valley and spin, γ_{vs}.

γ_{vs} connects the direct spin-allowed and indirect spin-forbidden state, which have, apart from possible exchange energies, the same energy. Since the phonon has to provide the wave-vector difference between the valleys, which is given by the K point of the lattice, there are no suited energy and momentum conserving phonon modes available and we would thus expect that γ_{vs} is small. γ_s connects direct spin-allowed and spin-forbidden states, which are split by Δ_{cb}, but have equal wave vector. This scattering process can occur via Γ point phonons of similar energy, such as the E'' or A' modes. However, phonon interactions couple to the orbital part of the wave functions, and spin can only be flipped via spin-orbit interaction. We are not aware of explicit calculations of the related scattering rates. γ_v connects the direct spin-allowed with the indirect spin-allowed state and the direct spin-forbidden with the indirect spin-forbidden state. Both have the energy difference Δ_{cb} and a momentum difference between the $-$K and $+$K point. Phonon modes matching the energy and momentum required for these transitions are present such that we expect γ_v to be the largest of all three rates.

In view of these properties of the excitonic states in SL-$MoSe_2$ we now discuss the observed FWM density dynamics, starting with $T = 77$ K. The optical excitation populates the direct spin-allowed exciton close to the center of the radiative cone. For linear polarization, a superposition of $X^{\uparrow\uparrow}_{++}$ and $X^{\downarrow\downarrow}_{--}$ is populated, while for circular polarization, only $X^{\uparrow\uparrow}_{++}$ is populated. In both cases, the states are expected to show a fast radiative recombination, consistent with the first component in Fig. 5. Its decay time of about 0.6 ps, observed for both polarizations, is consistent with the expected radiative lifetime. Importantly, a scattering towards other states would not be expected to change the signal so strongly, as the exciton-exciton interaction is not expected to be strongly affected, considering that the involved exciton kinetic energies are much smaller than the exciton binding energy. This scattering is therefore not expected to be prominent in the FWM signal. A competing process to radiative decay could be the phonon-assisted formation of a trion. The slightly decreasing τ_1 with power could be due to exciton-exciton scattering into the fast states or other spin-valley states.

Once the initially excited population of slow spin-allowed excitons is gone, the remaining fast excitons would be expected to have an effective radiative decay at least a thousand times slower, as calculated earlier, in the order of 1 ns. The fast excitons show, as discussed before, a large LT splitting, which is mixing the $X^{\uparrow\uparrow}_{++}$ and $X^{\downarrow\downarrow}_{--}$ states. The memory of the initially

excited state, which differs for circularly and linearly polarized excitation, is therefore lost in the fast direct states within the first picoseconds, and the subsequent dynamics is essentially independent of the excitation polarization configuration, consistent with our observations, see, e.g., Fig. 4. The dynamics given by the second component with times τ_2 of about 20 ps is therefore attributed to scattering of the fast spin-allowed states into the indirect spin-forbidden states, possibly via the indirect spin-allowed states involving the rates γ_v and γ_s, the latter being the smaller rate is expected to dominate the observed time scale. The resulting change of their interaction with the probed slow direct spin-allowed states changes the phase of the signal. Notably, the indirect spin-allowed and direct spin-forbidden states at about 20 meV higher energy will not carry a significant population at $T = 77$ K, considering the Boltzmann factor $\exp(-20/6.6) \approx 0.05$—they are thus only intermediate states facilitating the transfer between direct spin-allowed and indirect spin-forbidden state.

Once the population of the fast direct spin-allowed exciton states and indirect spin-forbidden excitons have thermalized by this process, the exciton density is decaying by scattering back to the direct spin-allowed state or nonradiative processes. This process is attributed to the third component with $\tau_3 \approx 300$ ps. The different FWM signal phases of the components can accordingly be attributed to the somewhat different exciton-exciton interactions with the slow direct spin-allowed states, which are carrying the FWM polarization. Component 1 is due to the interaction within these states, component 2 due to the interaction with fast direct spin-allowed states, and component 3 due to the interaction with indirect spin-forbidden excitons. Notably, the amplitudes of the components are scaling approximately with their decay rate, as would be expected for this picture of three exciton reservoirs with bidirectional scattering.

The increasing amplitude of the third process with excitation power could accordingly be related to exciton-exciton scattering from the direct spin-allowed to the indirect spin-forbidden state, which requires exchange of electron or hole in the process $X^{\uparrow\uparrow}_{++} + X^{\downarrow\downarrow}_{--} \longrightarrow X^{\uparrow\downarrow}_{+-} + X^{\downarrow\uparrow}_{-+}$. This could increase also the radiative decay by a faster scattering into the slow spin-allowed excitons.

The weak fourth component with an amplitude A_4 around 1% of A_1 has a time constant in the tens of nanoseconds and decreases its relative amplitude with increasing fluence. It could be related to thermalization of existing unpaired charge carriers after the optical excitation.

Lets us now interpret the temperature dependence. With increasing temperature, the occupation of the phonons creating the scattering γ_s and γ_v is increasing according to their Bose distribution. We can therefore expect that at 150 K and 300 K, these two rates are dominating the dynamics, providing a faster thermalization between the various exciton states.

At 150 K, this leads to an increased amplitude and reduced decay time of the third component. At 300 K, the overall signal is reduced, due to the homogeneous broadening of the exciton of about 40 meV, superseeding the inhomogeneous broadening (see also Fig. 1). This also means that the slow direct spin-allowed excitons are scattered within the pulse duration towards the other exciton states, and the dynamics is dominated by a single decay time around 30 ps. At this temperature, the mobility of excitons in the sample could also allow the excitons to recombine nonradiatively at defects. However, in Ref. [42], a similar sample did not show a strong variation of the nonresonantly excited PL intensity $T > 100$ K, indicating that diffusion to defects and subsequent nonradiative decay is not significant.

D. Exciton-exciton annihilation

Observation of exciton-exciton annihilation (EEA) in SL-TMD has been proposed to interpret carrier dynamics in WSe_2 [6], MoS_2 [7], and $MoSe_2$ [8], using largely varying EEA rates, and rates affected by the substrate [43], while there are also reports where EEA was not invoked [44,45]. In all these works, nonresonant optical excitation leading to free electron-hole pairs has been used. To evaluate whether EEA has a role in the dynamics we measure, we follow the analysis in Ref. [8] using the same delay range from 5 ps to 60 ps. The EEA rate equation describing the density decay is given by

$$\frac{dN}{dt} = -\frac{N}{\tau} - \frac{\gamma_A}{2}N^2 \tag{6}$$

with the density of excitons N, the low-density decay rate τ, and the EEA rate γ_A. In our experiments the exciton density is expected to be proportional to $S/\sqrt{P}$, where S is the FWM field amplitude. We therefore fit this quantity as shown in the inset of Fig. 9(a) for delays τ_{23} from 5 ps to 55 ps with the solution of Eq. (6) neglecting the low-density decay rate, given by [46]

$$N(t) = \left(N_0^{-1} + \gamma_A t/2\right)^{-1}, \tag{7}$$

where N_0 is the initial exciton density. The resulting rates γ_A are given in Fig. 9(a). We find that γ_A is strongly varying, being approximately inversely proportional to the power P. To avoid the approximation of negligible low-density rate used in Ref. [8], we divide Eq. (6) by $-N$, resulting in a linear dependence on N. We show the measured $-(dS/dt)/S$ as function of $S/\sqrt{P}$ in Fig. 9(c) for $\tau_{23} \geqslant 0.3$ ps, together with the same quantity deduced from the fit Eq. (4) to the data shown in Fig. 3. The linear dependence predicted by Eq. (6) does not describe the data. Furthermore, the data for different P do not overlap, as would be predicted by Eq. (6). Similar results were found for the aged sample using the data from Fig. 4. We therefore conclude that EEA is not significant in our experiments.

V. TRION POPULATION DYNAMICS

In order to investigate the trion X_A^- dynamics, we measured the population dynamics resonantly exciting and probing the X_A^- transition [see Fig. 1(b)] using cross-linearly polarized pumps at $T = 77$ K. The data are shown in Fig. 10(a) for two different powers. As in Sec. IV, we fitted the data using Eq. (4) with four decay processes, and the resulting decay times, amplitudes, and phases are shown in Fig. 10(b). We find an initial fast decay of $\tau_1 \approx 1$ ps similar to the exciton-resonant dynamics. The instantaneous response A_{nr} is stronger relative to A_1 and is inverse ($\varphi_{nr} \approx \pi$) to A_1. The stronger relative weight is expected considering the weaker X_A^- absorption and about 5 times smaller A_1 for a given power. The second time scale $\tau_2 \approx 5$ ps is shorter than for the exciton-resonant

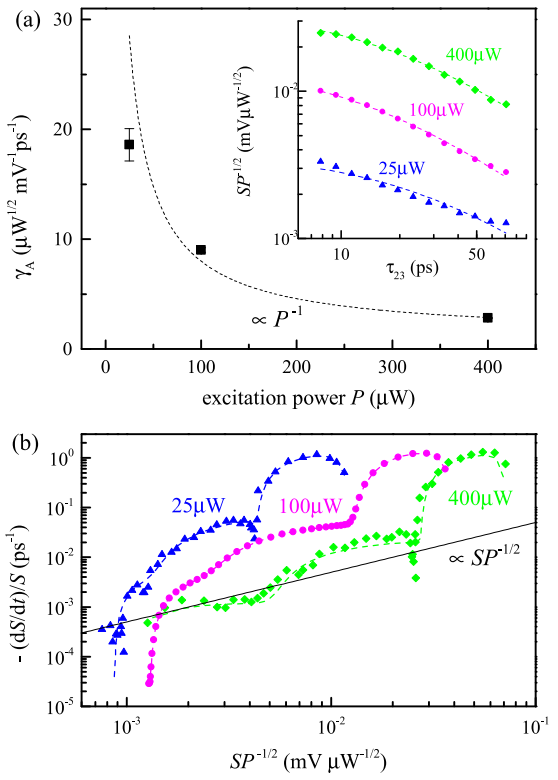

FIG. 9. Exciton-exciton annihilation analysis. (a) Inset: Normalized FWM field amplitude $S/\sqrt{P}$ (symbols) as function of τ_{23} for different powers P as indicated, and fits (dashed lines) according to Eq. (7). Main: γ_A values (squares) determined by the fit; dashed line: P^{-1} dependence. (b) Logarithmic decay rate of the FWM field amplitude S versus $S/\sqrt{P}$ for different P as indicated. Symbols: Measurements for $\tau_{23} \geqslant 0.3$ ps; dashed lines: Fits shown in Fig. 3. The solid line shows a dependence proportional to $S/\sqrt{P}$.

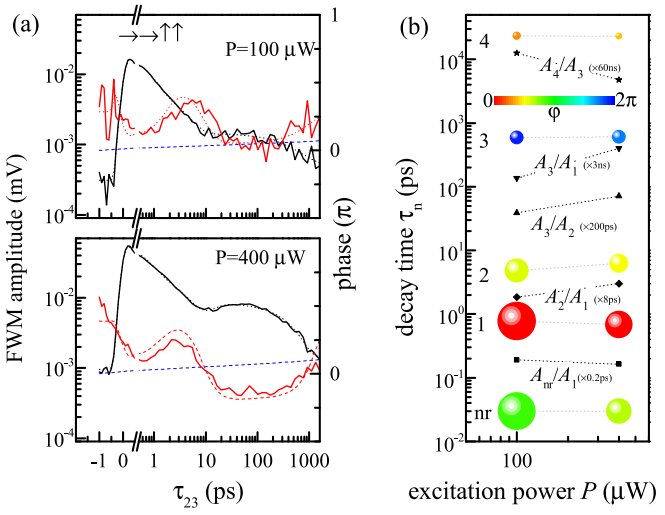

FIG. 10. Density dynamics of the fresh sample for excitation resonant to X_A^- at $T = 77$ K. (a) FWM field amplitude and phase as function of the delay τ_{23} for two excitation powers P as given and cross-linear polarization configuration $(\rightarrow,\rightarrow,\uparrow,\uparrow)$. The fitted phase drift (blue dashed line) has been subtracted from the data shown. (b) Results of a fit to (a), formatted as Fig. 5. For absolute scaling $A_1 = 24\ \mu$V at $P = 100\ \mu$W.

dynamics where $\tau_2 \approx 20$ ps and has a larger relative amplitude compared to A_1. The later dynamics given by τ_3 and τ_4 instead are similar to what is found for the exciton-resonant excitation. We do not observe a significant variation of the time scales with power, in contrast to what has been recently reported [27] and interpreted as saturation of defect states. The amplitudes slightly decrease with increasing power. All the amplitude ratios seem to increase with the power, with the exception of A_4/A_3. The phase evolution differs considerably from the exciton-resonant data—we find $\varphi_2 \approx \pi/2$ while $\varphi_3 \sim 2\pi$, equivalent to zero; φ_4 is slightly less then $\pi/2$. The similarity of the τ_3 and τ_4 values to the exciton-resonant results indicates that after about 100 ps, the initially excited X_A^- are thermalized with X_A, and thus the memory of the initially excited transition is lost.

Concerning the initial dynamics, we note that exciton to trion conversion has been recently investigated [47], showing a conversion within 1–2 ps at $T = 13$ K. At this temperature, the trion with a binding energy of 30 meV is not thermally excited, so the time measured is the trion formation time. We emphasize that the rate of the corresponding process exciton plus electron gives trion plus phonon is expected to be proportional to the electron density, and the latter was not given in Ref. [47]. The reported time scale should therefore be taken only as a possible value, which can vary strongly depending on the electron density.

In our experiment we initally excite X_A^-, and we are therefore measuring as initial process the thermal excitation of the trion within its dispersion and its ionization into a free electron and an exciton. The radiative recombination of trions is expected to be much slower than the slow bright excitons, due to the momentum distribution of the remaining electron after the decay [21]. We therefore attribute the first time scale τ_1 to trion thermalization within its dispersion, as trion ionization is not expected to be efficient at $T = 77$ K, due to the large trion binding energy of 30 meV compared to the thermal energy. The second time scale τ_2 should then be attributed to trion ionization, a process which was recently observed in photoluminescence [48]. After ionization, the dynamics are expected to be similar to the case of exciton excitation, and in fact we see similar time scales. The phases differ somewhat due to the difference in energy of the probed optical response.

VI. CONCLUSIONS

In conclusion, we have measured the exciton dephasing and density dynamics in SL-$MoSe_2$ using resonant excitation, which is avoiding the excitation of free electron-hole pairs. We determined at $T = 77$ K a dephasing time of 0.36 ps for the exciton and 0.27 ps for the trion. The measured density dynamics from 100 fs to 10 ns shows four distinct processes which we interpreted in terms of the intrinsic band structure as radiative decay, scattering within the exciton dispersion, and scattering between spin-allowed direct and spin-forbidden indirect excitons. Exciton-exciton annihilation was excluded as relevant process in the dynamics. The data presented in this work are available from the Cardiff University data archive [49].

ACKNOWLEDGMENTS

This work was partially funded by the EPSRC under Grant No. EP/M020479/1. A.I.T. and E.M.A. thank the financial support of the EPSRC Grant No. EP/M012727/1, Graphene Flagship under Grant No. 696656, and ITN Spin-NANO under Grant No. 676108. W.L. thanks J. Kasprzak for helpful discussions. F.W. acknowledges support from the Royal Academy of Engineering.

[1] K. F. Mak, C. Lee, J. Hone, J. Shan, and T. F. Heinz, Phys. Rev. Lett. **105**, 136805 (2010).

[2] A. Splendiani, L. Sun, Y. Zhang, T. Li, J. Kim, C.-Y. Chim, G. Galli, and F. Wang, Nano Lett. **10**, 1271 (2010).

[3] D. Xiao, G.-B. Liu, W. Feng, X. Xu, and W. Yao, Phys. Rev. Lett. **108**, 196802 (2012).

[4] K. F. Mak, K. He, J. Shan, and T. F. Heinz, Nat. Nanotechnol. **7**, 494 (2012).

[5] M. M. Ugeda, A. J. Bradley, S.-F. Shi, F. H. da Jornada, Y. Zhang, D. Y. Qiu, W. Ruan, S.-K. Mo, Z. Hussain, Z.-X. Shen, F. Wang, S. G. Louie, and M. F. Crommie, Nat. Mater. **13**, 1091 (2014).

[6] S. Mouri, Y. Miyauchi, M. Toh, W. Zhao, G. Eda, and K. Matsuda, Phys. Rev. B **90**, 155449 (2014).

[7] D. Sun, Y. Rao, G. A. Reider, G. Chen, Y. You, L. Brézin, A. R. Harutyunyan, and T. F. Heinz, Nano Lett. **14**, 5625 (2014).

[8] N. Kumar, Q. Cui, F. Ceballos, D. He, Y. Wang, and H. Zhao, Phys. Rev. B **89**, 125427 (2014).

[9] Z. Y. Zhu, Y. C. Cheng, and U. Schwingenschlögl, Phys. Rev. B **84**, 153402 (2011).

[10] K. Kośmider, J. W. González, and J. Fernández-Rossier, Phys. Rev. B **88**, 245436 (2013).

[11] X.-X. Zhang, Y. You, S. Y. F. Zhao, and T. F. Heinz, Phys. Rev. Lett. **115**, 257403 (2015).

[12] G.-B. Liu, W.-Y. Shan, Y. Yao, W. Yao, and D. Xiao, Phys. Rev. B **88**, 085433 (2013).

[13] H. Dery and Y. Song, Phys. Rev. B **92**, 125431 (2015).

[14] A. Zhang, J. Fan, Y. Li, J. Ji, G. Zhao, T. Xia, T. Yan, X. Zhang, W. Zhang, X. Wang, and Q. Zhang, arXiv:1503.08631.

[15] S. Dufferwiel, T. P. Lyons, D. D. Solnyshkov, A. A. P. Trichet, F. Withers, S. Schwarz, G. Malpuech, J. M. Smith, K. S. Novoselov, M. S. Skolnick, D. N. Krizhanovskii, and A. I. Tartakovskii, arXiv:1612.05073.

[16] C. Robert, D. Lagarde, F. Cadiz, G. Wang, B. Lassagne, T. Amand, A. Balocchi, P. Renucci, S. Tongay, B. Urbaszek, and X. Marie, Phys. Rev. B **93**, 205423 (2016).

[17] M. Selig, G. Berghuser, A. Raja, P. Nagler, C. Schller, T. F. Heinz, T. Korn, A. Chernikov, E. Malic, and A. Knorr, Nat. Commun. **7**, 13279 (2016).

[18] G. Moody, J. Schaibley, and X. Xu, J. Opt. Soc. Am. B **33**, C39 (2016).

[19] H. Yu, G.-B. Liu, P. Gong, X. Xu, and W. Yao, Nat. Commun. **5**, 3876 (2014).

[20] J. S. Ross, S. Wu, H. Yu, N. J. Ghimire, A. M. Jones, G. Aivazian, J. Yan, D. G. Mandrus, D. Xiao, W. Yao, and X. Xu, Nat. Commun. **4**, 1474 (2013).

[21] A. Esser, E. Runge, R. Zimmermann, and W. Langbein, Phys. Rev. B **62**, 8232 (2000).

[22] M. Sidler, P. Back, O. Cotlet, A. Srivastava, T. Fink, M. Kroner, E. Demler, and A. Imamoglu, Nat. Phys. **13**, 255 (2017).

[23] S. Horzum, H. Sahin, S. Cahangirov, P. Cudazzo, A. Rubio, T. Serin, and F. M. Peeters, Phys. Rev. B **87**, 125415 (2013).

[24] A. Singh, G. Moody, S. Wu, Y. Wu, N. J. Ghimire, J. Yan, D. G. Mandrus, X. Xu, and X. Li, Phys. Rev. Lett. **112**, 216804 (2014).

[25] G. Wang, E. Palleau, T. Amand, S. Tongay, X. Marie, and B. Urbaszek, App. Phys. Lett. **106**, 112101 (2015).

[26] T. Jakubczyk, V. Delmonte, M. Koperski, K. Nogajewski, C. Faugeras, W. Langbein, M. Potemski, and J. Kasprzak, Nano Lett. **16**, 5333 (2016).

[27] F. Gao, Y. Gong, M. Titze, R. Almeida, P. M. Ajayan, and H. Li, Phys. Rev. B **94**, 245413 (2016).

[28] P. Borri and W. Langbein, in *Semiconductor Quantum Bits*, edited by O. Benson and F. Henneberger (World Scientific, Singapore, 2009).

[29] J. Shah, *Ultrafast Spectroscopy of Semiconductors and Semiconductor Nanostructures* (Springer, Berlin, 1996), Chap. 2.

[30] F. Masia, N. Accanto, W. Langbein, and P. Borri, Phys. Rev. Lett. **108**, 087401 (2012).

[31] N. Accanto, F. Masia, I. Moreels, Z. Hens, W. Langbein, and P. Borri, ACS Nano **6**, 5227 (2012).

[32] A. Naeem, F. Masia, S. Christodoulou, I. Moreels, P. Borri, and W. Langbein, Phys. Rev. B **91**, 121302 (2015).

[33] A. Arora, K. Nogajewski, M. Molas, M. Koperski, and M. Potemski, Nanoscale **7**, 20769 (2015).

[34] Y. N. Gartstein, X. Li, and C. Zhang, Phys. Rev. B **92**, 075445 (2015).

[35] H. Wang, C. Zhang, W. Chan, C. Manolatou, S. Tiwari, and F. Rana, Phys. Rev. B **93**, 045407 (2016).

[36] L. C. Andreani and F. Bassani, Phys. Rev. B **41**, 7536 (1990).

[37] L. C. Andreani, *Confined Electrons and Photons: New Physics and Applications* (Plenum Press, New York, 1995), pp. 57–112.

[38] S. Dufferwiel, S. Schwarz, F. Withers, A. Trichet, F. Li, M. Sich, O. D. Pozo-Zamudio, C. Clark, A. Nalitov, D. Solnyshkov, G. Malpuech, K. Novoselov, J. Smith, M. Skolnick, D. Krizhanovskii, and A. Tartakovskii, Nat. Commun. **6**, 8579 (2015).

[39] V. Savona and W. Langbein, Phys. Rev. B **74**, 075311 (2006).

[40] R. Zimmermann, E. Runge, and V. Savona, in *Quantum Coherence, Correlation and Decoherence in Semiconductor Nanostructures*, edited by T. Takagahara (Elsevier Science, New York, 2003), p. 89.

[41] R. Zimmermann, W. Langbein, E. Runge, and J. M. Hvam, Physica E **10**, 40 (2001).

[42] T. Godde, D. Schmidt, J. Schmutzler, M. Aßmann, J. Debus, F. Withers, E. M. Alexeev, O. D. Zamudio, O. V. Skrypka, K. S. Novoselov, M. Bayer, and A. I. Tartakovskii, Phys. Rev. B **94**, 165301 (2016).

[43] Y. Yu, Y. Yu, C. Xu, A. Barrette, K. Gundogdu, and L. Cao, Phys. Rev. B **93**, 201111(R) (2016).

[44] H. Shi, R. Yan, S. Bertolazzi, J. Brivio, B. Gao, A. Kis, D. Jena, H. G. Xing, and L. Huang, ACS Nano **7**, 1072 (2013).
[45] H. Wang, C. Zhang, and F. Rana, Nano Lett. **15**, 339 (2015).
[46] In the solution given in Ref. [9], Eq. (3), a factor $1/2$ is missing.
[47] A. Singh, G. Moody, K. Tran, M. E. Scott, V. Overbeck, G. Berghäuser, J. Schaibley, E. J. Seifert, D. Pleskot, N. M. Gabor, J. Yan, D. G. Mandrus, M. Richter, E. Malic, X. Xu, and X. Li, Phys. Rev. B **93**, 041401(R) (2016).
[48] A. M. Jones, H. Yu, J. R. Schaibley, J. Yan, D. G. Mandrus, T. Taniguchi, K. Watanabe, H. Dery, W. Yao, and X. Xu, Nat. Phys. **12**, 323 (2016).
[49] Cardiff University data archive. http://doi.org/10.17035/d.2017.0037144365